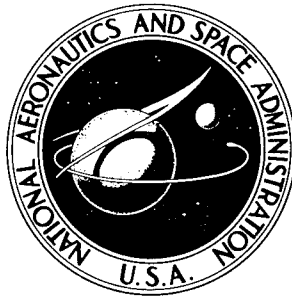
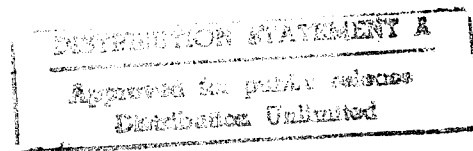


NASA TECHNICAL NOTE



NASA TN D-3465

NASA TN D-3465



19960419 042

EXPLORATORY INVESTIGATION OF THE EFFECT OF NYLON GRAIN SIZE ON ABLATION OF PHENOLIC NYLON

by Gerald D. Walberg and Roger K. Crouch

Langley Research Center

Langley Station, Hampton, Va.

QUALITY INSPECTED 1

NATIONAL AERONAUTICS AND SPACE ADMINISTRATION • WASHINGTON, D. C. • AUGUST 1965

DEPARTMENT OF DEFENSE
PLASTICS TECHNICAL EVALUATION CENTER
PICATINNY ARSENAL, DOVER, N. J.

PLASTICS

DISCLAIMER NOTICE



**THIS DOCUMENT IS BEST
QUALITY AVAILABLE. THE
COPY FURNISHED TO DTIC
CONTAINED A SIGNIFICANT
NUMBER OF PAGES WHICH DO
NOT REPRODUCE LEGIBLY.**

EXPLORATORY INVESTIGATION OF THE EFFECT OF
NYLON GRAIN SIZE ON ABLATION OF PHENOLIC NYLON

By Gerald D. Walberg and Roger K. Crouch

Langley Research Center
Langley Station, Hampton, Va.

NATIONAL AERONAUTICS AND SPACE ADMINISTRATION

For sale by the Clearinghouse for Federal Scientific and Technical Information
Springfield, Virginia 22151 - Price \$2.00

EXPLORATORY INVESTIGATION OF THE EFFECT OF NYLON GRAIN SIZE ON ABLATION OF PHENOLIC NYLON

By Gerald D. Walberg and Roger K. Crouch
Langley Research Center

SUMMARY

[An exploratory investigation of the effect of nylon grain size on the ablation of phenolic nylon has been carried out. Ablation models which differed only with respect to nylon grain size were tested in air and in nitrogen at stream stagnation temperatures from 2300° R to 3600° R (1278° K to 2000° K), a stream stagnation pressure of approximately 100 psia (0.69 MN/m²), and a Mach number of approximately 2. Two series of models were tested. The models in the first series contained nylon particles having dimensions larger than 0.0098 inch (0.25 mm) and those in the second series contained nylon particles having dimensions smaller than 0.0017 inch (0.043 mm). The results obtained from these tests showed that the mechanical strength of the char layers produced and the resistance of these chars to removal by aerodynamic and chemical mechanisms were greater for the small-grain material than for the large-grain material.]

INTRODUCTION

It is now generally agreed that, for certain reentry trajectories, the so-called charring ablators may provide thermal protection superior to that obtainable from either subliming or liquid layer ablators. The superiority of the charring ablator is, however, dependent on the thermal and mechanical properties of its char layer. If, for instance, the char layer were removed by oxidation, spallation, or aerodynamic erosion, the ablator's efficiency would be markedly reduced. It is of interest, then, to relate the characteristics of a given unpyrolyzed material to the characteristics of the char layer produced by thermal degradation of the material.

Although the mechanism of pyrolysis is, at best, poorly understood, some investigations of the relations between the characteristics of a char layer and the plastic from which it was formed have been reported. In reference 1, for instance, it is argued that, in the case of a nylon-cloth—phenolic-resin laminate, the geometry of the nylon fibers determines, in large measure, the geometry of the resulting char layer. This argument is based on an examination of char-layer photomicrographs which show that a carbonaceous wall is built up around the individual nylon fibers. In view of the evidence

presented in reference 1, it is reasonable to expect that, in the case of a powdered-nylon—phenolic-resin material, the char-layer geometry (and, hence, the ablation characteristics of the materials) should be influenced by the grain size of the nylon. The purpose of the present investigation was to confirm or disprove this expectation.

In the present investigation, two series of powdered-nylon—phenolic-resin test specimens were subjected to a Mach 2 airstream which had a stagnation pressure of approximately 100 psia (0.69 MN/m^2), and stagnation temperatures from 2300° R to 3600° R (1278° K to 2000° K). The first series of test specimens contained nylon having a grain size larger than 0.0098 inch (0.25 mm), and the second series contained nylon having a grain size smaller than 0.0017 inch (0.043 mm). Both series of test specimens were also tested in nitrogen in an effort to determine the importance of oxidation as a char-removal mechanism.

SYMBOLS

The units used for the physical quantities defined in this section are given in both U.S. Customary Units and in the International System of Units (SI). (See ref. 2.)

c	specific heat, British thermal units/pound- $^\circ \text{R}$ (joules/kilogram- $^\circ \text{K}$)
H	heat of pyrolysis, British thermal units/pound (joules/kilogram)
h	stagnation enthalpy, British thermal units/pound (joules/kilogram)
h_D	enthalpy transported by diffusion (see eq. (A1)), British thermal units/pound (joules/kilogram)
N_{Le}	Lewis number
l	model length, inches (meters)
\dot{l}	rate of change with time of model length, inches/second (meters/second)
M	Mach number
\dot{m}	rate of mass removal or of mass flow, pounds/foot 2 -second (kilograms/meter 2 -second)
p	pressure, pounds/inch 2 (newtons/meter 2)

q	heat flux, British thermal units/foot ² -second (watts/meter ²)
R	gas constant for air, 1716 feet ² /second ² -°R (287 joules/kilogram-°K)
r	hemispherical nose radius, feet (meters)
T	temperature, °R (°K)
t	model exposure time, seconds
u	velocity in boundary layer parallel to model surface, feet/second (meters/second)
x	meridional distance along model surface measured from stagnation point, feet (meters)
ε	emissivity of char surface
η	transpiration cooling factor
μ	viscosity, pound-seconds/foot ² (newton-seconds/meter ²)
ρ	density, slugs/foot ³ (kilograms/meter ³) or pounds/foot ³ (kilograms/meter ³)
σ	Stefan-Boltzmann constant, British thermal units/foot ² -second-°R ⁴ (watts/meter ² -°K ⁴)

Subscripts:

a	at pyrolysis interface
b	pebble bed used to heat test gas
C	cold wall
c	char layer
e	evaluated at outer edge of boundary layer

g	gaseous products injected into boundary layer
o	condition of material prior to testing
ox	due to oxidation reactions
pg	gaseous products evolved during pyrolysis of virgin plastic
t	free-stream stagnation conditions
t,2	stagnation conditions behind a normal shock wave
vp	virgin plastic
w	conditions in boundary layer at model surface
∞	free-stream conditions

APPARATUS

Test Facility

The tests reported herein were carried out in the Mach 2 ceramic-heated jet at the Langley Research Center. In this facility the test gas (either air or nitrogen for the present tests) is passed through a ceramic pebble-bed heat exchanger where it is heated to stagnation temperatures of 2300° R to 3600° R (1278° K to 2000° K). The test gas is then expanded through a contoured $M = 2$ nozzle and exhausted to the atmosphere. Details of the facility are presented in reference 3.

Models

Model details are shown in figure 1, and a photograph of the ablation model is presented as figure 2. The models were simple hemisphere-cylinders which were machined from large blocks of phenolic nylon. These blocks were molded from equal parts (by weight) of powdered phenolic resin and powdered nylon. The process by which the phenolic nylon was molded is the same as that described for high-density phenolic nylon in reference 4. The models differed only with respect to the grain size of the powdered nylon. The models referred to herein as "large-grain models" contained nylon which had grains larger than 0.0098 inch (0.25 mm), and the "small-grain models" contained nylon which had grains smaller than 0.0017 inch (0.043 mm). The construction, dimensions, and properties of the models are presented in table I and figures 1 and 2. The

char densities and virgin-plastic densities presented in table I were determined by using water-immersion (Archimedes' principle) techniques. Care was taken to seal the specimens with an acrylic plastic coating so that water absorption would not influence the results of these measurements.

Instrumentation

Although the test specimens themselves were not instrumented, considerable facility instrumentation was used in an effort to determine test conditions and test-specimen behavior. This instrumentation consisted of high-speed (approximately 400 frames per second) motion-picture cameras which provided information regarding test-specimen recession rates and surface behavior, an optical pyrometer which was used to measure the temperature of the ceramic pebble bed, a photographic pyrometer (described in ref. 5) which was used to measure test-specimen surface temperature, and two differential pressure transducers which were used to measure stagnation pressures in the settling chamber of the pebble heater and in the free jet test region (behind a normal shock wave). Signals from the pressure transducers were fed to a recording oscillograph. Micro-switches located on the test-specimen inserter produced signals which caused a "shift" on the oscillograph record when the test specimen was inserted into and retracted from the jet; thus, an accurate measure of test-specimen exposure time was provided.

TESTS

The following test procedure was used in the present investigation: with the model retracted from the jet stream, the pebble bed was heated to a desired temperature. The appropriate working gas (either air or nitrogen) was then allowed to flow through the hot pebble bed and, thence, through the Mach 2 nozzle. A pressure regulator maintained the desired pressure in the pebble bed. Once a hot gas flow had been established through the nozzle, the model was inserted in the jet stream. During its exposure, the model was photographed by motion-picture cameras and by the photographic pyrometer. After an exposure of approximately 6 seconds, the model was retracted from the stream. Large-grain and small-grain models were tested in air at nominal stagnation temperatures of 2300°R (1278°K), 3000°R (1667°K), and 3600°R (2000°K) and in nitrogen at nominal stagnation temperatures of 2300°R (1278°K) and 3600°R (2000°K). The tests in air were carried out at a nominal stagnation pressure of 107 psia (0.74 MN/m^2). The tests in nitrogen were carried out at stagnation pressures from 92 psia (0.63 MN/m^2) to 112 psia (0.77 MN/m^2). A series of stagnation-pressure probes was tested in both air and nitrogen to determine the stagnation pressure behind a normal shock in the jet test region. Test conditions are presented in table II. The stream stagnation temperatures T_t presented in table II were calculated by using facility calibration curves

(stagnation-temperature probe data) and the measured values of the pebble-bed temperature T_b . The Mach numbers presented in table II and figure 3 were computed from measured values of p_t (pressure in the pebble bed) and $p_{t,2}$ (total pressure behind the normal shock). In these computations, data of reference 6 were used and appropriate corrections for the caloric imperfection of the test stream were made. The cold-wall aerodynamic heating rates presented in table II were computed by using an approximate simplified form of the Fay and Riddell expression (ref. 7). The equations used in calculating heating rates are presented in an appendix to this paper.

The nozzle used in this investigation was contoured to be shock-free at Mach 2, and the data presented in figure 3 show that, throughout the stagnation-temperature range of the present tests, actual Mach numbers were within 10 percent of this design value. Furthermore, the test stagnation pressures (table II) were such that the nozzle was, for all practical purposes, fully expanded when exhausting to the atmosphere. Hence, it is believed that the present tests were carried out in a uniform, constant Mach number stream which was free of any strong shock or expansion waves.

In any pebble-bed facility, such as the one used in this investigation, a certain amount of dust (zirconia particles) will be lifted from the pebble bed and will be present in the test stream. In the present tests, zirconia bombardment produced observable gouges in the char layers of the test models and undoubtedly caused some erosion of the char surfaces. Data, which are subsequently presented, show, however, that char recession caused by dust was, in all instances, small compared with the char recession caused by oxidation. Finally, calibration tests have shown that, when proper operating procedures are used, the bombardment of models by dust does not vary significantly within a given test or from test to test, and the present investigation was therefore essentially a comparison of the response of two materials to the same environment (i.e., the large- and small-grain materials were both subjected to similar zirconia bombardment). Hence, the overall results of this study are comparative in nature and were not significantly affected by the presence of zirconia dust in the airstream.

RESULTS AND DISCUSSION

Appearance of Models During and After Tests

As mentioned previously, high-speed motion pictures were taken during the present tests. Selected frames from these motion pictures are presented in figures 4 and 5, where the models are shown being tested in air and in nitrogen, respectively. These photographs were selected as representing the typical behavior of the models at the indicated test conditions. It should be pointed out that varying combinations of filters and f-stops were used in taking these motion pictures, and because of this the brightness of the

models presented in figures 4 and 5 is not an accurate indication of relative surface temperatures. During the tests in air at a nominal stagnation temperature of 3600°R (2000°K), the large-grain models experienced a mechanical char failure whereby discrete fragments were removed from the char surface and swept downstream. This char failure is illustrated by figure 4(c) where the same photograph is shown both normally exposed and overexposed. In the overexposed photograph, the trajectories of the small char fragments appear as streaks. Figure 4(f) presents normally exposed and overexposed photographs of a small-grain model being tested under similar conditions. As can be seen, no char failure such as occurred on the large-grain models was observed for the small-grain models.

The model behavior in air and in nitrogen was quite dissimilar. The most significant difference was that the nose recession was obviously less in nitrogen. Also, at a given stagnation temperature, the models were less luminous in nitrogen than in air. The models tested in nitrogen developed rough nose surfaces which had relatively deep gouges, apparently caused by the impacts of small zirconia particles present in the gas stream. (See figs. 5(a) and 5(c).) In air, on the other hand, little evidence of zirconia bombardment was seen. Apparently, the relatively rapid ablation of the models in air effectively erased any gouges cut by zirconia particles. Another difference between the air and nitrogen tests was that the char layers produced in nitrogen were thick compared with those produced in air and developed large surface irregularities. (See fig. 5(d).) Occasionally these surface irregularities became large enough to cause the removal of sizable pieces of char by local aerodynamic forces. Such a removal is shown in figure 5(b). No char failure such as that observed on the large-grain models in air (fig. 4(c)) was observed on either large- or small-grain models in nitrogen. When the models which had been tested in nitrogen at $T_t \approx 3600^{\circ}\text{R}$ (2000°K) were retracted from the stream, the thick char layers which had been developed were blown off the model nose. It is speculated that this removal was caused by pressure differences produced in the char as the model crossed the jet boundary. No such removal was observed after the air tests.

Photographs of the models, taken after the tests, are presented in figure 6. These photographs are presented primarily to show the differences between the chars produced by the large- and small-grain materials. The small-grain char had a crazed appearance with relatively large flakes separated by fissures which extended from the char surface to the pyrolysis interface. Within each flake, the pores of the small-grain char appear to be small and uniformly distributed. On the other hand, the large-grain chars have the general appearance of a sponge. Although some fissures are evident in the large-grain char (see figs. 6(e) and 6(f)), they are small compared with those present in the small-grain char. The porosity of the large-grain char is open in nature and most of the pores are relatively large. Comparisons of figures 6(f) and 6(h) and of 6(c) and 6(g) show that

the appearance of the char is virtually independent of the chemical composition of the test stream – that is, whether the stream is composed of air or of nitrogen.

In an effort to determine the thickness of char layers and degradation zones, the models were sectioned and photographed. Photographs of typical sections are presented in figure 7. The outermost layer of material is the carbonaceous char. The lighter band between the char layer and the virgin plastic is a degradation zone within which the material has been partially pyrolyzed. When the models were sectioned, significant quantities of char were lost in the vicinity of the saw cut. Also, as can be seen in figure 7, the char layers are quite thin and the definition of an interface between the char and the degradation zone or between the degradation zone and the virgin plastic is difficult, especially for the large-grain material. As a result of these difficulties, the most accurate statement that can be made regarding the stagnation-region char thicknesses of the models tested in air is that the chars developed by both the large- and small-grain materials at $T_t \approx 2300^\circ \text{R}$ (1278°K), $\approx 3000^\circ \text{R}$ (1667°K), and $\approx 3600^\circ \text{R}$ (2000°K) were all approximately 0.01 inch (0.254 mm) thick. Since the char layers produced in nitrogen at $T_t \approx 3600^\circ \text{R}$ (2000°K) were blown off when the models were retracted from the stream, no measurements of char thickness were possible. The char fragments remaining on the models (see figs. 7(c) and 7(d)) do, however, show that the chars produced in nitrogen at $T_t \approx 3600^\circ \text{R}$ (2000°K), were much thicker than those produced in air, and estimates made from the motion pictures indicate that the stagnation-region char thicknesses after exposure to the nitrogen stream were approximately 0.01 inch (0.254 mm) at $T_t \approx 2300^\circ \text{R}$ (1278°K) and 0.1 inch (2.54 mm) at $T_t \approx 3600^\circ \text{R}$ (2000°K).

Measurements taken from the photograph indicated stagnation-region degradation-zone thicknesses of approximately 0.005 inch (0.127 mm) for the small-grain models tested in air. Degradation-zone thicknesses which varied from 0.01 inch (0.254 mm) at $T_t \approx 2300^\circ \text{R}$ (1278°K) to 0.02 inch (0.508 mm) at $T_t \approx 3600^\circ \text{R}$ (2000°K) were measured from near the stagnation points of the small-grain models tested in nitrogen. As can be seen from figure 7, no definite interface exists between the degradation zone and the large-grain virgin material. In general, however, the degradation zone for the large-grain material seems to be slightly thicker than that for the small-grain material.

Another observation that can be made from figure 7 is that the phenolic-nylon material appears to be a suspension of nylon grains in a matrix of phenolic resin. This appearance suggests that no significant chemical reaction between the nylon and the phenolic resin took place during the molding operation.

Measured Char Surface Temperatures

Char surface temperatures are presented as a function of model exposure time in figure 8. As mentioned previously, these surface temperatures were measured with a

photographic pyrometer. It has been estimated (ref. 5) that for most applications this pyrometer is capable of measuring surface temperatures from 1800°F to 3600°F (1255°K to 2255°K) with a precision of 2 percent. During the present investigation, however, the models tested in nitrogen developed irregular char surfaces which made the reading of the pyrometer films difficult and produced considerable uncertainties ($\pm 200^{\circ}\text{R}$ or $\pm 111^{\circ}\text{K}$) in the char surface temperature for the nitrogen tests. This uncertainty is indicated in figure 8 by a hatched region surrounding the data points for the nitrogen tests. The repeated symbols in figure 8 at a given time indicate measurements taken at various points on the model nose. The data presented in figure 8 show that the char surface temperatures measured in air were essentially constant over the stagnation region of the model nose and that these temperatures were essentially independent of exposure time for times greater than 1 second. The char surfaces of the models tested at $T_t \approx 2300^{\circ}\text{R}$ (1278°K) (both in air and in nitrogen) did not reach temperatures high enough to be measured by the pyrometer used in this investigation. A range of char surface temperatures for these tests can, however, be established as follows: the lowest temperature that can be measured by the pyrometer is approximately 2260°R (1256°K); hence, the char surface temperatures must have been less than 2260°R (1256°K). During the tests in air at $T_t \approx 2300^{\circ}\text{R}$ (1278°K), the char surfaces exhibited a reddish orange glow. Since the emissivities of iron oxide and carbon are comparable and since, according to reference 9, a piece of iron when heated in air to a temperature of approximately 2000°R (1111°K) will exhibit a reddish orange color, it may be assumed that the char surface temperatures were $\approx 2000^{\circ}\text{R}$ ($\approx 1111^{\circ}\text{K}$). Accordingly (see fig. 8), the char surface temperatures in air at $T_t \approx 2300^{\circ}\text{R}$ (1278°K) have been assumed to be between 2000°R (1111°K) and 2260°R (1256°K). The models tested in nitrogen at $T_t \approx 2300^{\circ}\text{R}$ (1278°K) did not glow. Hence, the only statement that can be made about their char surface temperatures is that they were less than 2260°R (1256°K).

The data presented in figure 8 show that, at a stream stagnation temperature of 3600°R (2000°K), the models tested in air were significantly hotter than those tested in nitrogen. As a matter of fact, these data show char surface temperatures, for the tests in air, which are significantly higher than the stream stagnation temperature. These high surface temperatures are caused by the exothermic heat release of the char oxidation reactions which, as shown in a subsequent section of this paper, is comparable in magnitude to the cold-wall convective heat flux to the models. These data also show that, of the models tested in air, the large-grain models were hotter than the small-grain models.

Char Recession Rates

From the high-speed motion pictures taken during the tests, model lengths were measured and are presented as a function of time in figure 9. The data presented in

figures 9(a) and 9(b) show that, with the exception of a short transient period near the beginning of each test, the models tested in air experienced an approximately linear variation of length with time. These constant recession rates together with the constant char surface temperatures shown in figure 8 and the thin char layers indicated in figure 7(a) suggest that steady-state ablation was obtained during the tests made in air. The data for the nitrogen tests (figs. 9(c) and 9(d)) show that the model length changed only slightly during the tests at $T_t \approx 2300^\circ \text{R}$ (1278°K). During the tests at $T_t \approx 3600^\circ \text{R}$ (2000°K) the length of the models decreased gradually during most of the test and then decreased suddenly near the end of the test. This sudden decrease in length indicates the removal of a large piece of char. This type of char removal was discussed previously and illustrated in figure 5(b). These data indicate that the ablation in nitrogen is transient in nature with a continually changing char thickness and ablation rate.

Char recession rates were determined by measuring the model lengths at successive times from the color motion pictures taken during the tests, plotting these lengths in figure 9, fairing straight lines through these data (see fig. 9), and measuring the slopes of the faired lines. The char recession rates thus obtained are presented as functions of stream stagnation temperature in figure 10. From figure 10 it is seen that the char removal rates in air were significantly larger and more strongly dependent on stagnation temperature than those in nitrogen. It is also seen that, in both air and nitrogen, the large-grain char receded faster than the small-grain char.

Effect of Nylon Grain Size On Char-Layer

Composition and Geometry

From the photographs presented in figure 7 it is seen that the virgin plastic appears to be a suspension of nylon grains in phenolic resin, that is, no chemical reaction between the nylon and the phenolic during the molding process is apparent. Also, as shown in table I the chars produced by both the large- and small-grain materials had the same densities. This equality of densities implies that the same amount of char was produced by the decomposition of a unit mass of either large- or small-grain material. Comparison of the size and distribution of nylon particles shown in figure 7 with the size and distribution of char-layer pores shown in figure 6 suggests that each pore resulted from the melting and subsequent vaporization of an individual nylon particle. Hence, it appears that the char-layer geometry (pore size and distribution) was determined to a large extent by the grain size of the nylon, but that the mass of char produced by a unit mass of virgin plastic and the chemical composition of the char were not affected by the grain size of the nylon.

Relative Strength of Large-Grain and

Small-Grain Char Layers

From the data presented in figure 10, it is seen that the large-grain char receded faster (i.e., was removed more rapidly) than the small-grain char at all stream temperatures, in both air and nitrogen. From the motion pictures taken during the tests, it was seen that during the air tests at $T_t \approx 3600^\circ \text{ R}$ (2000° K) the large-grain char suffered a mechanical failure (removal of small fragments from the char surface), whereas the small-grain char did not. Furthermore, examination of the models after testing showed that the large-grain char was easier to remove than the small-grain char. Finally, data presented in reference 10 show that the strength of porous carbon decreases with increasing pore size. From these findings, it appears that the mechanical strength of the large-grain char was less than that of the small-grain char.

Effect of Stream Composition On Ablative

Heat Balance and Char Removal

During the analysis of the data obtained in the present tests, an attempt was made to satisfy the following steady-state ablative heat balance:

$$q_C \left(1 - \frac{h_w}{h_e}\right) + q_{ox} - \sigma \epsilon T_C^4 = \dot{m}_{vp} \left\{ H + \left[\left(\frac{\rho_c}{\rho_{vp}} \right) c_c + \left(\frac{\rho_{vp} - \rho_c}{\rho_{vp}} \right) c_{pg} \right] (T_c - T_a) \right. \\ \left. + c_{vp} (T_a - T_o) + \eta \frac{\dot{m}_g}{\dot{m}_{vp}} (h_e - h_w) \right\}$$

A steady-state heat balance similar to the foregoing equation is derived in reference 11. Approximate values for the heat flux due to oxidation q_{ox} were determined for tests 1, 2, and 3 (small-grain models) and 5, 6, and 7 (large-grain models) by using the foregoing heat-balance equation, the values of H_c , c_{vp} , T_a , T_o , c_c , c_{pg} , η , and \dot{m}_g/\dot{m}_{vp} presented in table III, the values of T_c , h_e , h_w , and \dot{m}_{vp} presented in table II, and the values of ρ_c and ρ_{vp} presented in table I. The resulting values for q_{ox} are presented in figure 11. The hatched areas in the figure indicate the previously discussed uncertainty in char surface temperature for the $T_t \approx 2300^\circ \text{ R}$ (1278° K) tests. From figure 11 it is seen that the heat flux due to oxidation is comparable in magnitude to the cold-wall aerodynamic heat flux (see table II) and hence constituted a major part of the heat input to models tested in air. The data presented in figure 11 also show that the heat flux due to oxidation was larger for the large-grain models than for the small-grain models. The material properties presented in table III were compiled from the literature and are admittedly approximate. Although alternate sets of material properties may produce changes in the calculated values of q_{ox} , it is the opinion of the authors that

no realistic set of properties will produce results qualitatively different from those presented in figure 11.

From figure 10 it is seen that the char removal rates were significantly higher in air than in nitrogen. These observations together with the results presented in figure 11 suggest that the principal char removal mechanism during the air tests was oxidation. Accordingly, diffusion-controlled char oxidation rates were calculated by using the steady-state equations presented in reference 8. These theoretical rates are compared with the measured char removal rates in figure 12. The horizontal bars shown on the nitrogen-test data points in figure 12 reflect the uncertainty in char surface temperature for the nitrogen tests (see previous discussion and fig. 8). Note that, although the test results show a stronger dependence on surface temperature than is predicted by theory, the quantitative agreement is reasonably good for the small-grain models. The dependence on surface temperature shown by the test data may indicate that the char oxidation reaction is not completely diffusion controlled. In general, however, the data presented in figure 12 indicate that the major char-removal mechanism of the small-grain material was oxidation. For the large-grain material, figure 12 shows that oxidation was an important contributor to char removal, but that significant quantities of char were removed by other mechanisms. Most important among these other char-removal mechanisms was the mechanical char failure shown in figure 4(c).

CONCLUDING REMARKS

An exploratory investigation of the effect of nylon grain size on the ablation of phenolic nylon has been carried out. The results of this investigation showed a definite relation between the nylon grain size, the appearance of the char layers produced, and the ability of these char layers to resist removal by aerodynamic and chemical mechanisms.

The appearance of the chars suggests that the pores in the char were produced by the melting and subsequent vaporization of individual nylon particles. Hence, the char pore size increases as the size of the nylon particles increases. Results obtained from tests in air and in nitrogen at nominal stream stagnation temperatures from 2300° R to 3600° R (1278° K to 2000° K) showed that at all test conditions the char recession rates for the large-grain material were higher than those for the small-grain material. Examinations of the test models and of data obtained from the literature suggest that these higher recession rates are due, in part, to the large-grain char being mechanically weaker than the small-grain char. Analysis of the results obtained from the tests in air and in nitrogen showed that during the tests carried out in air, char oxidation reactions contributed a significant part of the heat flux to the char surface and were responsible for the major part of the char removal experienced by the small-grain models. This analysis

also showed that char removal from the large-grain models was partly due to oxidation and partly due to a mechanical char failure whereby small particles were removed from the char surface.

Langley Research Center,
National Aeronautics and Space Administration,
Langley Station, Hampton, Va., March 10, 1966.

APPENDIX

METHOD USED IN CALCULATING AERODYNAMIC HEATING RATES

For an equilibrium, laminar, stagnation-region boundary layer, the following expression for the aerodynamic heat flux is given in reference 7:

$$q = 30.3(\rho_w \mu_w)^{0.1}(\rho_e \mu_e)^{0.4} \left[1 + (N_{Le}^{0.52} - 1) \frac{hD}{h_e} \right] (h_e - h_w) \sqrt{\frac{du_e}{dx}} \quad (A1)$$

When the Lewis number is assumed to be equal to unity and the modified Newtonian expression for the stagnation-point velocity gradient on a hemisphere is substituted into equation (A1), the following expression is obtained:

$$q = 30.3(\rho_w \mu_w)^{0.1}(\rho_e \mu_e)^{0.4} (h_e - h_w) \frac{\left[\frac{2(p_e - p_\infty)}{\rho_e} \right]^{0.25}}{r^{0.5}} \quad (A2)$$

where r is the radius of the hemispherical nose. By using the perfect gas law, the densities in equation (A2) can be expressed in terms of pressure and temperature as follows:

$$\rho = \frac{p}{RT} \quad (A3)$$

Hence, equation (A2) becomes

$$\frac{q}{(h_e - h_w) \sqrt{p_w}} = \frac{36.1}{R^{0.25}} \left(\frac{\mu_w}{T_w} \right)^{0.1} \left(\frac{\mu_e}{T_e} \right)^{0.4} T_e^{0.25} \left(1 - \frac{p_\infty}{p_e} \right)^{0.25} \quad (A4)$$

In the calculation of heating rates for the present investigation, equation (A4) was used, the Sutherland equation was used to compute viscosities, the term $\left(1 - \frac{p_\infty}{p_e} \right)^{0.25}$ was computed by using the curves and tables presented in reference 6, and the gas constant R was assumed to be $1716 \text{ ft}^2/\text{sec}^2\text{-}^\circ\text{R}$ ($287 \text{ J}/^\circ\text{K}\text{-kg}$). The cold-wall heating rates presented in table II were computed for $T_w = 540^\circ \text{ R}$ (300° K).

REFERENCES

1. Marolo, Samuel A.: Microstructure of Ablative Plastic Chars. WADD Tech. Rept. 60-856, Feb. 1961.
2. Mechtly, E. A.: The International System of Units - Physical Constants and Conversion Factors. NASA SP-7012, 1964.
3. Fields, E. M.; Hopko, Russell N.; Swain, Robert L.; and Trout, Otto F., Jr.: Behavior of Some Materials and Shapes in Supersonic Free Jets at Stagnation Temperatures up to $4,210^{\circ}$ F, and Descriptions of the Jets. NACA RM L57K26, 1958.
4. Wilson, R. Gale (Compiler): Thermophysical Properties of Six Charring Ablators From 140° to 700° K and Two Chars From 800° To 3000° K. NASA TN D-2991, 1965.
5. Exton, Reginald J.: Theory and Operation of a Variable Exposure Photographic Pyrometer Over the Temperature Range 1800° to 3600° F (1255° to 2255° K). NASA TN D-2660, 1965.
6. Ames Research Staff: Equations, Tables, and Charts for Compressible Flow. NACA Rept. 1135, 1953.
7. Fay, J. A.; and Riddell, F. R.: Theory of Stagnation Point Heat Transfer in Dissociated Air. J. Aeron. Sci., vol. 25, no. 2, Feb. 1958, pp. 73-85, 121.
8. Walberg, Gerald D.: Analytical Study of Diffusion-Controlled Char Oxidation And Its Effects On Steady-State Ablation Of Plastic Materials. NASA TR R-242, 1966.
9. Baumeister, Theodore, ed.: Marks' Mechanical Engineers' Handbook. Sixth ed., McGraw-Hill Book Co., Inc., 1958.
10. Perry, John H.: Chemical Engineers' Handbook. Third ed., McGraw-Hill Book Co., Inc., 1950, p. 1550.
11. Barriault, R. J.; and Yos, J.: Analysis of the Ablation of Plastic Heat Shields That Form a Charred Surface Layer. ARS J., vol. 30, no. 9, Sept. 1960, pp. 823-829.

TABLE I.- ABLATION MODEL PROPERTIES

	Small-grain material	Large-grain material
Percent resin (by weight)	50	50
Percent nylon (by weight)	50	50
Type of resin	Union Carbide Bakelite BRP-5549	Union Carbide Bakelite BRP-5549
Type of nylon	DuPont Zytel 103	DuPont Zytel 103
Nylon grain size, in.	<0.0017	>0.0098
Nylon grain size, mm	<0.043	>0.25
Virgin-plastic density, lbm/ft ³	75	75
Virgin-plastic density, kg/m ³	1201	1201
Char density, lb/ft ³	20	20
Char density, kg/m ³	320	320
Model diameter, in.	0.375	0.375
Model diameter, mm	9.53	9.53
Model length, in.	1.156 to 1.190	1.160 to 1.228
Model length, cm	2.936 to 3.023	2.946 to 3.119

TABLE II.- TEST CONDITIONS

(a) U.S. Customary Units

Test	Test medium	Type of test (a)	T_b , °R	P_t , lb/in. ²	Test duration, t, sec	T_t , °R	M_∞ (b)	q_C , Btu/ft ² -sec (c)	T_C , °R	h_e , Btu/lbm (d)	h_w , Btu/lbm (d)	\dot{m}_{vp} , lbm/ft ² -sec
1	AIR	SG	2430	107	6.15	2300	1.96	306	<2260	591	<571	0.150
2	↓	↓	3430	↓	5.92	2980	1.94	455	2800	799	744	.181
3	↓	↓	4310	↓	5.97	3580	1.85	614	3760	983	1038	.230
4	↓	↓	4340	↓	6.00	3600	1.84	610	3760	989	1038	(e)
5	↓	LG	2440	↓	6.90	2310	1.96	308	<2260	594	<571	.176
6	↓	↓	3370	↓	6.03	2940	1.94	445	2800	787	744	.248
7	↓	↓	4340	↓	5.98	3600	1.84	609	4020	989	1118	.338
8	N ₂	SG	2510	92	6.20	2360	1.96	298	<2260	609	<571	(e)
9	↓	↓	4300	98	6.17	3575	1.85	581	(f)	(e)	(e)	↓
10	↓	↓	2430	112	6.11	2300	1.96	316	<2260	591	<571	↓
11	↓	↓	4310	95	6.00	3580	1.85	575	(f)	(e)	(e)	↓
12	↓	LG	2540	94	6.01	2385	1.96	308	<2260	617	<571	↓
13	↓	LG	4310	89	5.74	3575	1.85	551	(f)	(e)	(e)	↓
14	AIR	P	2400	107	10.24	2280	^c 2.01	(e)	(e)	↓	↓	↓
15	↓	↓	3410	107	(e)	2975	1.89	↓	↓	↓	↓	↓
16	↓	↓	4340	107	(e)	3600	1.79	↓	↓	↓	↓	↓
17	N ₂	↓	2420	111	2.51	2300	1.87	↓	↓	↓	↓	↓
18	↓	↓	2490	99	(e)	2320	2.02	↓	↓	↓	↓	↓
19	↓	↓	3460	96	(e)	3000	1.97	↓	↓	↓	↓	↓
20	↓	↓	4480	93	(e)	3680	1.86	↓	↓	↓	↓	↓
21	↓	↓	2540	93	1.96	2385	1.88	↓	↓	↓	↓	↓

(b) SI Units

Test	Test medium	Type of test (a)	T_b , °K	P_t , kN/m ²	Test duration, t, sec	T_t , °R	M_∞ (b)	q_C , MW/m ² (c)	T_C , °K	h_e , MJ/kg (d)	h_w , MJ/kg (d)	\dot{m}_{vp} , kg/m ² -sec
1	AIR	SG	1350	738	6.15	1278	1.96	3.47	<1256	1.37	<1.33	0.732
2	↓	↓	1906	↓	5.92	1656	1.94	5.16	1556	1.86	1.73	.883
3	↓	↓	2394	↓	5.97	1989	1.85	6.97	2089	2.28	2.41	1.122
4	↓	↓	2411	↓	6.00	2000	1.84	6.92	2089	2.30	2.41	(e)
5	↓	LG	1356	↓	6.90	1283	1.96	3.50	<1256	1.38	<1.33	.859
6	↓	↓	1872	↓	6.03	1633	1.94	5.05	1556	1.83	1.73	1.210
7	↓	↓	2411	↓	5.98	2000	1.84	6.91	2233	2.30	2.60	1.649
8	N ₂	SG	1394	634	6.20	1311	1.96	3.38	<1256	1.42	<1.33	(e)
9	↓	↓	2389	676	6.17	1986	1.85	6.59	(f)	(e)	(e)	↓
10	↓	↓	1350	772	6.11	1278	1.96	3.59	<1256	1.37	<1.33	↓
11	↓	↓	2394	655	6.00	1989	1.85	6.53	(f)	(e)	(e)	↓
12	↓	LG	1411	648	6.01	1325	1.96	3.50	<1256	1.43	<1.33	↓
13	↓	LG	2394	614	5.74	1986	1.85	6.25	(f)	(e)	(e)	↓
14	AIR	P	1333	738	10.24	1267	^c 2.01	(e)	(e)	↓	↓	↓
15	↓	↓	1894	738	(e)	1653	1.89	↓	↓	↓	↓	↓
16	↓	↓	2411	738	(e)	2000	1.79	↓	↓	↓	↓	↓
17	N ₂	↓	1344	765	2.51	1278	1.87	↓	↓	↓	↓	↓
18	↓	↓	1383	683	(e)	1289	2.02	↓	↓	↓	↓	↓
19	↓	↓	1922	662	(e)	1667	1.97	↓	↓	↓	↓	↓
20	↓	↓	2489	641	(e)	2044	1.86	↓	↓	↓	↓	↓
21	↓	↓	1411	641	1.96	1325	1.88	↓	↓	↓	↓	↓

^aSG small-grain material; LG large-grain material; P pressure probe.^bFrom figure 3.^cComputed values.^dGas at outer edge of boundary layer assumed to be thermodynamically identical to air.^eData not obtained.^fSee figure 9.

TABLE III.- MATERIAL PROPERTIES USED IN EVALUATING
ABLATIVE HEAT BALANCE

H	500 Btu/lbm (1.162 MJ/kg)
c _c	0.5 Btu/lbm-°R (2.09 J/kg-°K)
c _{vp}	0.4 Btu/lbm-°R (1.67 kJ/kg-°K)
c _{pg}	0.5 Btu/lbm-°R (2.09 kJ/kg-°K)
T _a	1500° R (833° K)
T _o	540° R (300° K)
η	0.7
\dot{m}_g/\dot{m}_{vp}	0.9
σ	4.806×10^{-13} Btu/ft ² -sec-°R ⁴ (5.4543 nW/m ² -°K ⁴)
ε	0.8

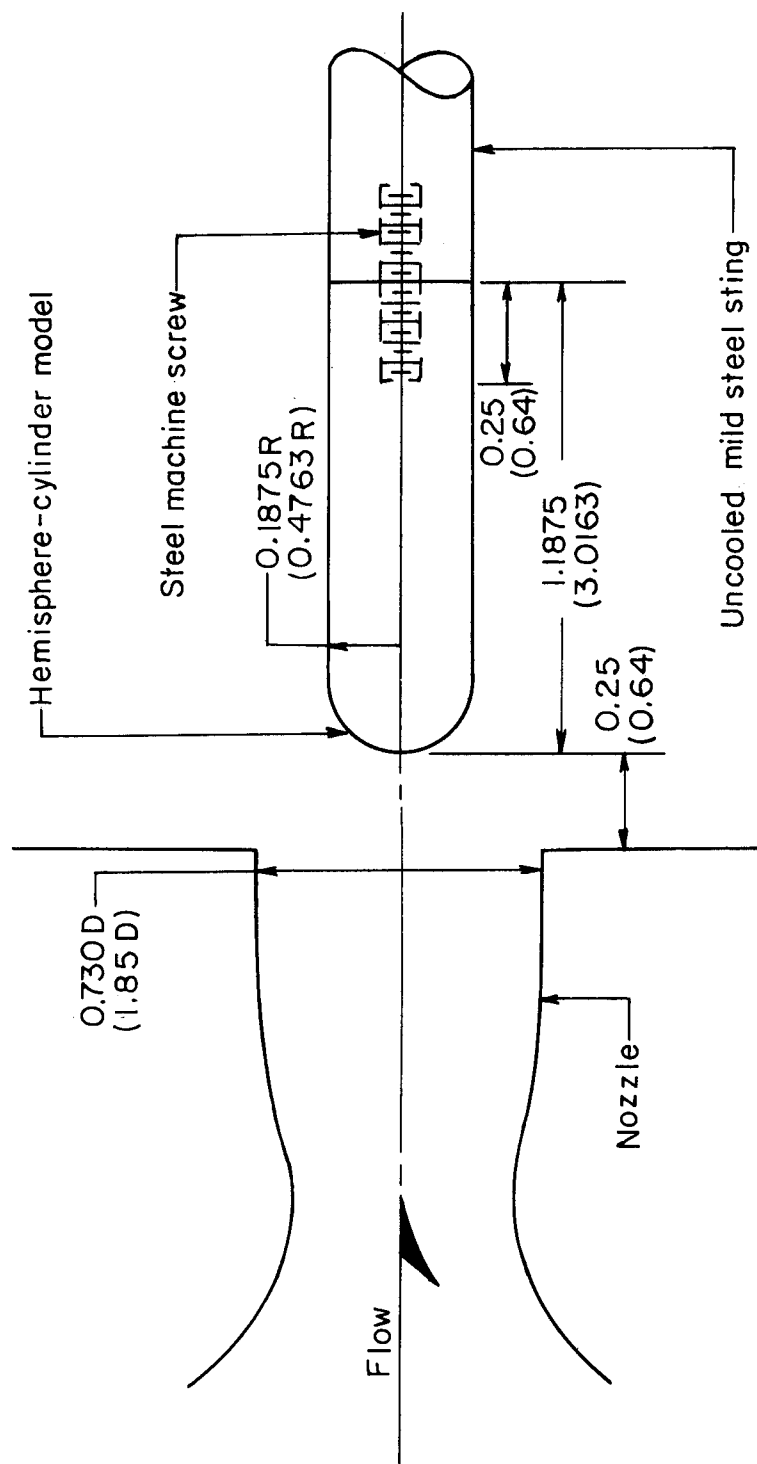


Figure 1.- Sketch of ablation specimen in test section of Mach 2 ceramic-heated jet. Dimensions are in inches (centimeters).

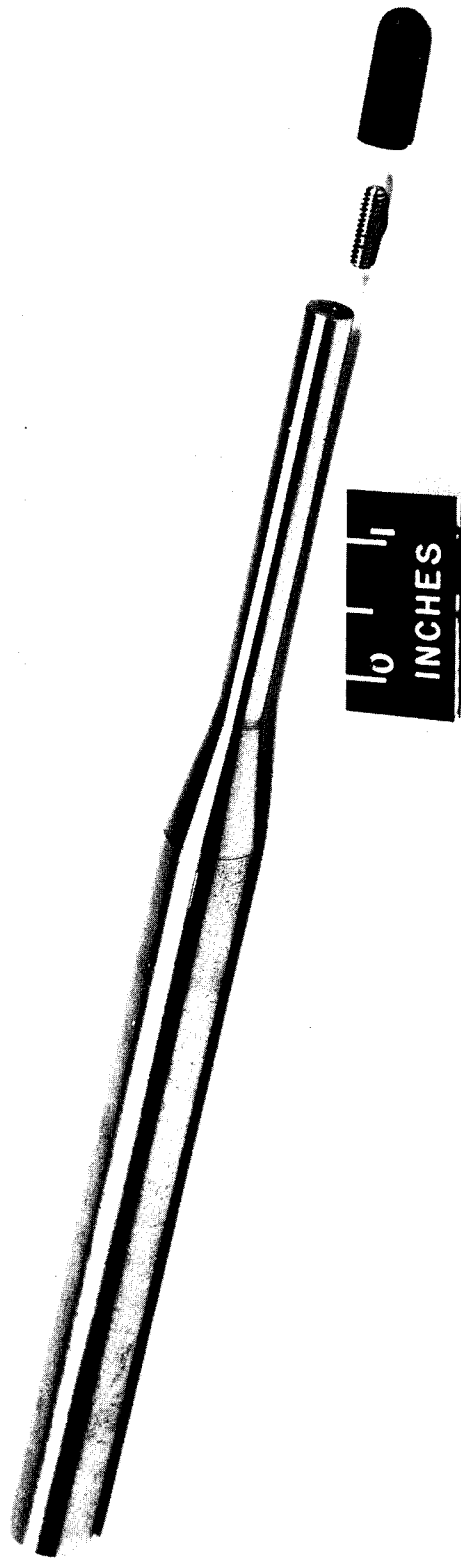


Figure 2.- Photograph of ablation model.

L-64-7890

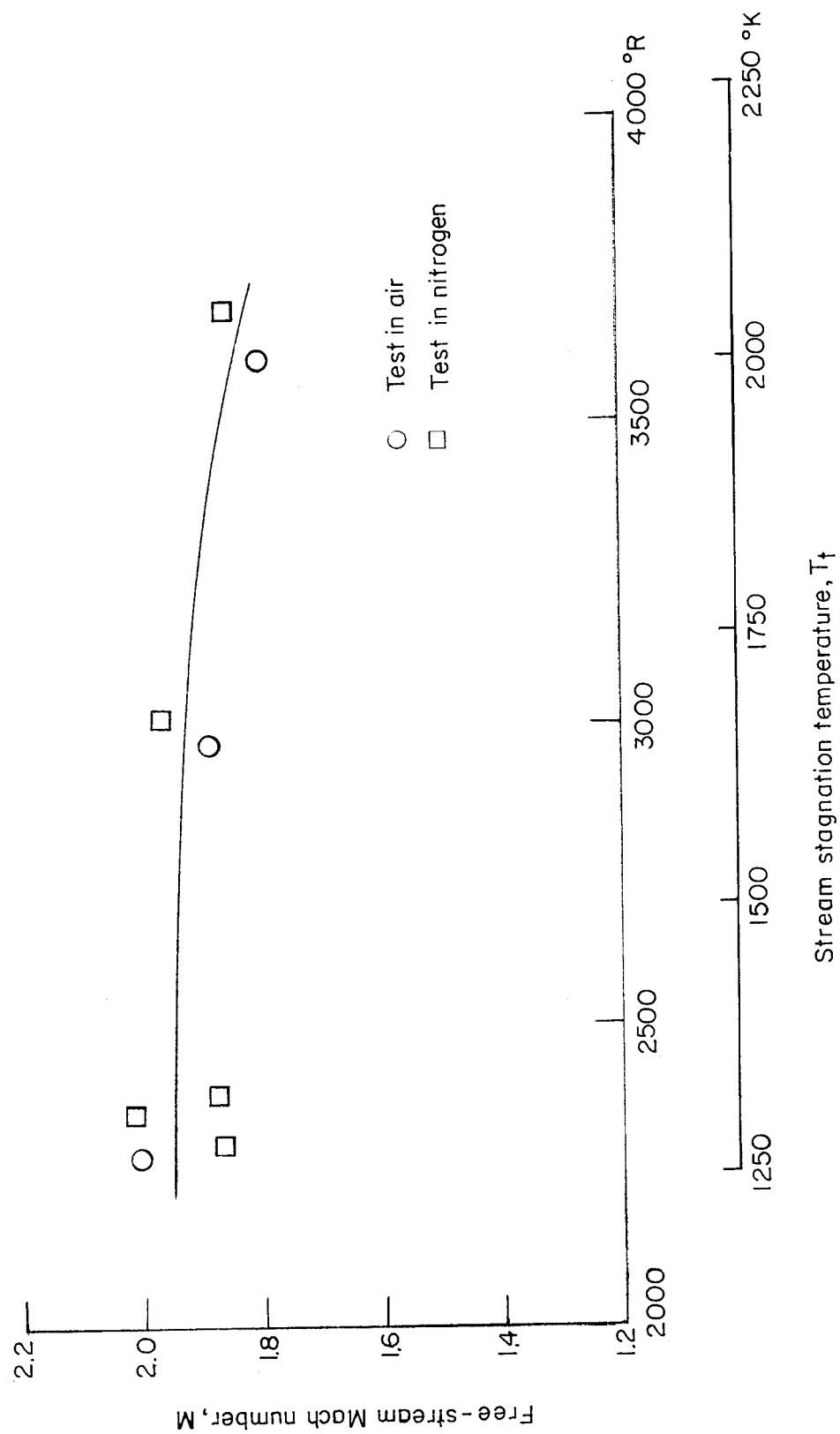
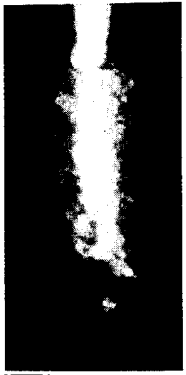


Figure 3:- Variation of free-stream Mach number with stream stagnation temperature.

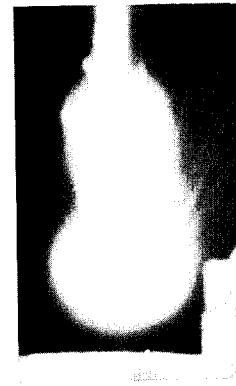
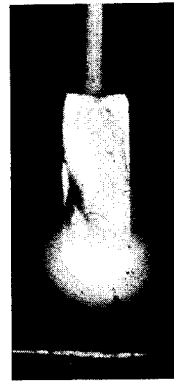
Large-grain models



(a) Test 5;
 $T_t = 2310^{\circ} \text{ R}$
 (1283° K) .



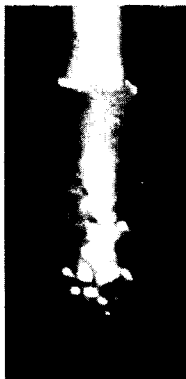
(b) Test 6;
 $T_t = 2940^{\circ} \text{ R}$
 (1633° K) .



Normal exposure Over exposed

(c) Test 7;
 $T_t = 3600^{\circ} \text{ R}$
 (2000° K) .

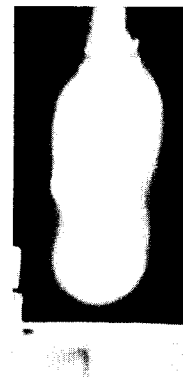
Small-grain models



(d) Test 1;
 $T_t = 2300^{\circ} \text{ R}$
 (1278° K) .



(e) Test 2;
 $T_t = 2980^{\circ} \text{ R}$
 (1656° K) .



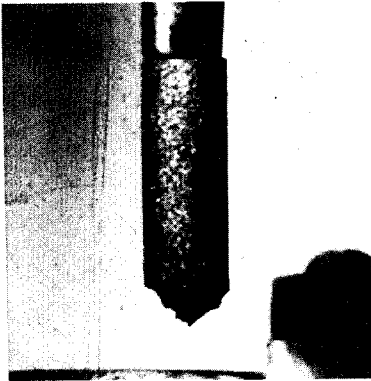
Normal exposure Over exposed

(f) Test 3;
 $T_t = 3580^{\circ} \text{ R}$
 (1989° K) .

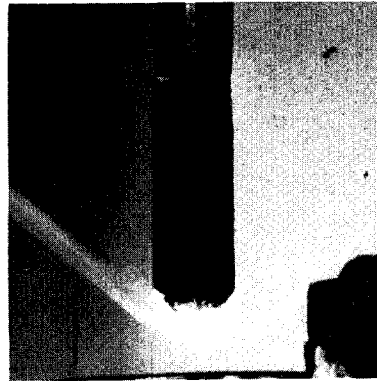
Figure 4.- Photographs of typical models being tested in air.

L-66-1113

Large-grain models

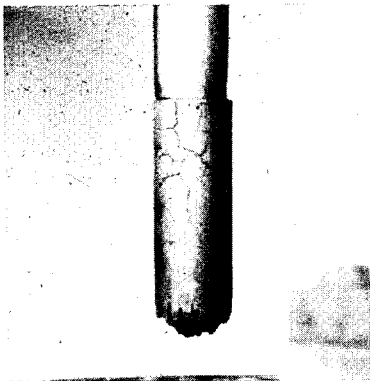


(a) Test 12;
 $T_t = 2385^{\circ} \text{R}$
(1325°K).

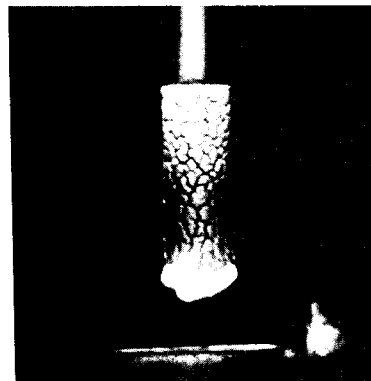


(b) Test 13;
 $T_t = 3575^{\circ} \text{R}$
(1986°K).

Small-grain models



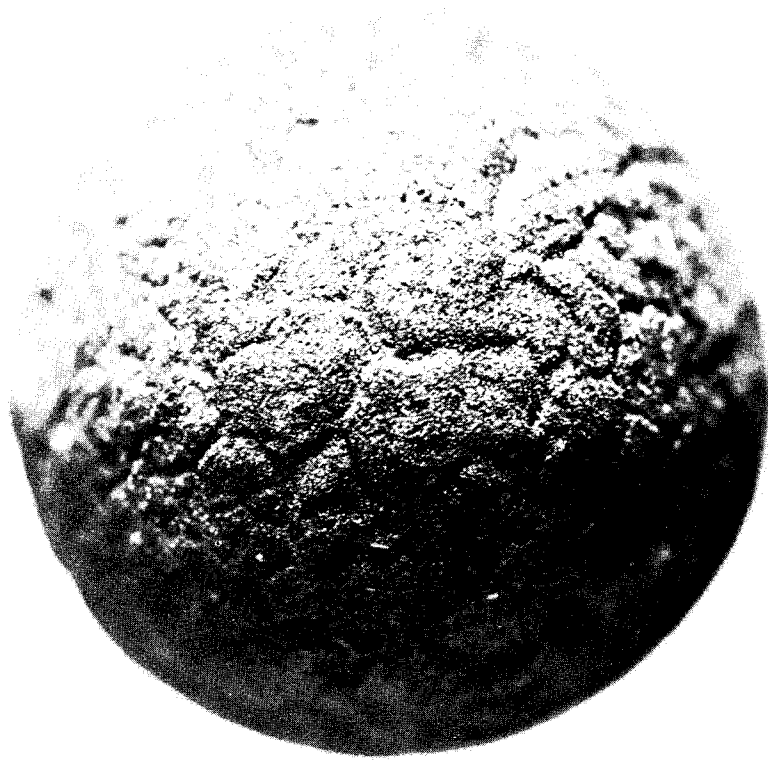
(c) Test 8;
 $T_t = 2360^{\circ} \text{R}$
(1311°K).



(d) Test 9;
 $T_t = 3575^{\circ} \text{R}$
(1986°K).

Figure 5.- Photographs of typical models being tested in nitrogen.

L-66-1114



(a) Test 1; small-grain model tested in air; $T_t = 23000\text{ R (12780 K)}$; $t = 6.15\text{ sec}$.

Figure 6.- Photographs of specimens after testing in Mach 2 ceramic-heated jet.

L-66-1115



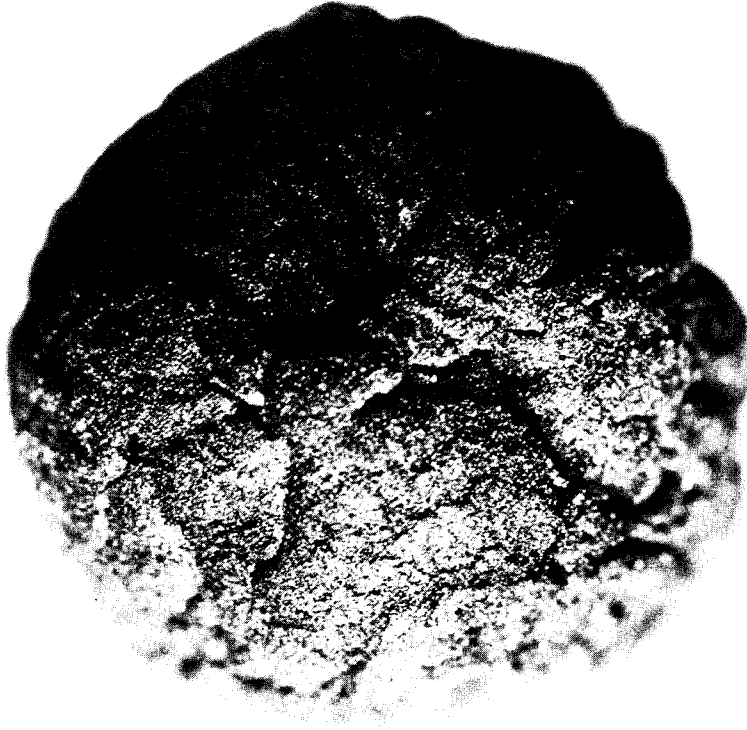
(b) Test 2; small-grain model tested in air; $T_t = 2980^\circ \text{R}$ (1656°K); $t = 5.92 \text{ sec.}$

L-66-1116

Figure 6.- Continued.

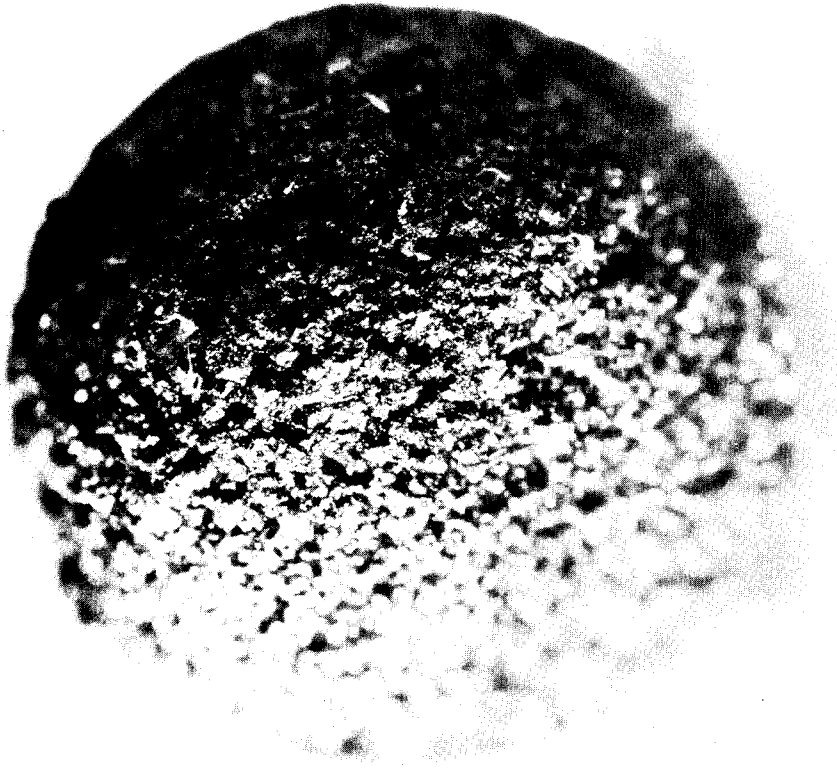
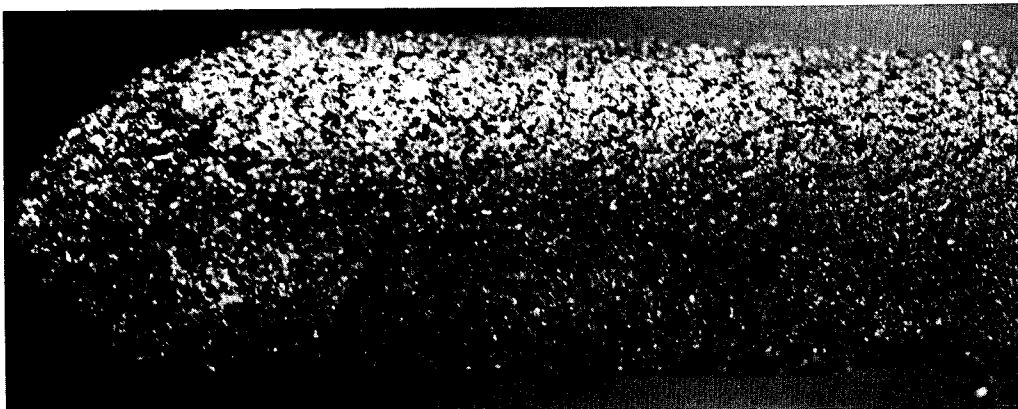


(c) Test 3; small-grain model tested in air; $T_t = 3580^\circ \text{R}$ (1989°K); $t = 5.97 \text{ sec.}$



L-66-1117

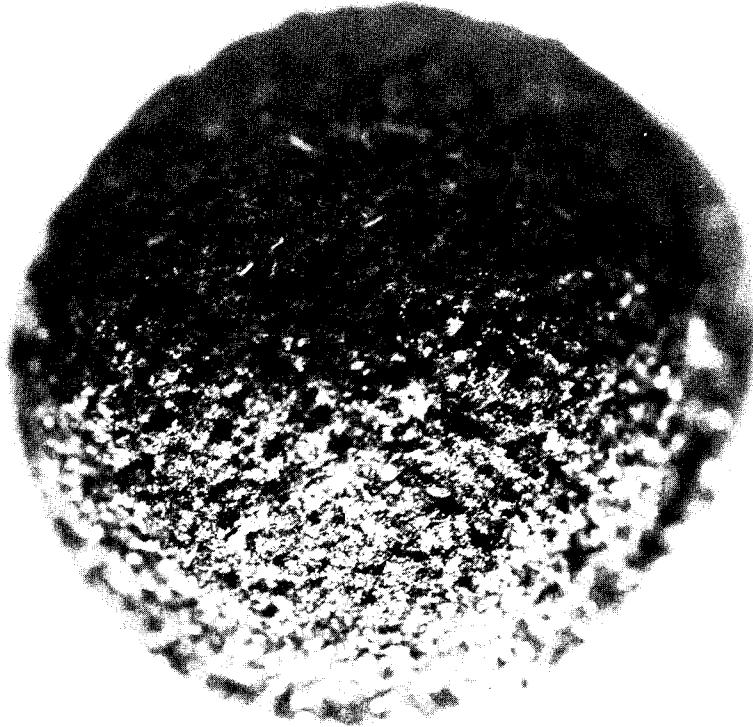
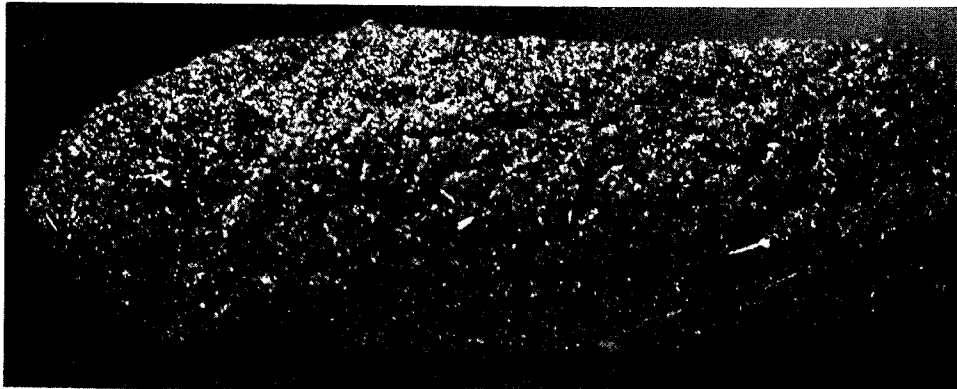
Figure 6.- Continued.



(d) Test 5; large-grain model tested in air; $T_t = 2310^\circ \text{R}$ (1283°K); $t = 6.90 \text{ sec.}$

Figure 6.- Continued.

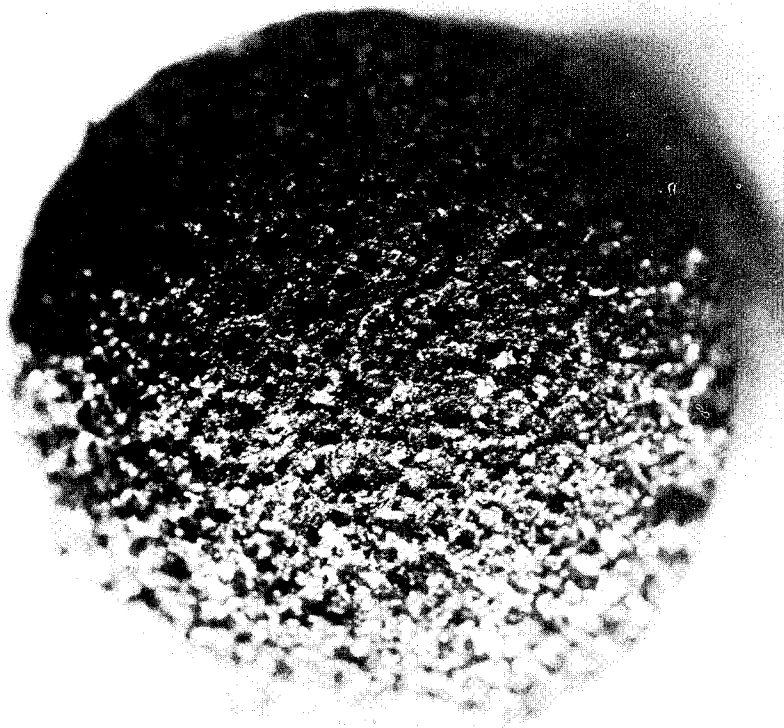
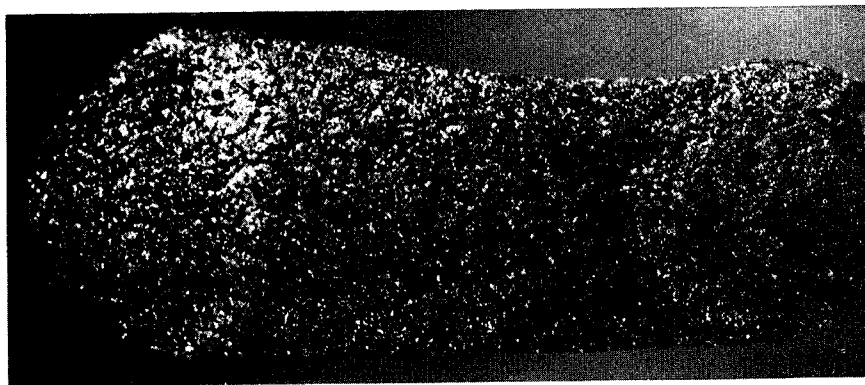
L-66-1118



(e) Test 6, large-grain model tested in air; $T_t = 2940^\circ \text{R}$ (1633°K); $t = 6.03 \text{ sec.}$

Figure 6.- Continued.

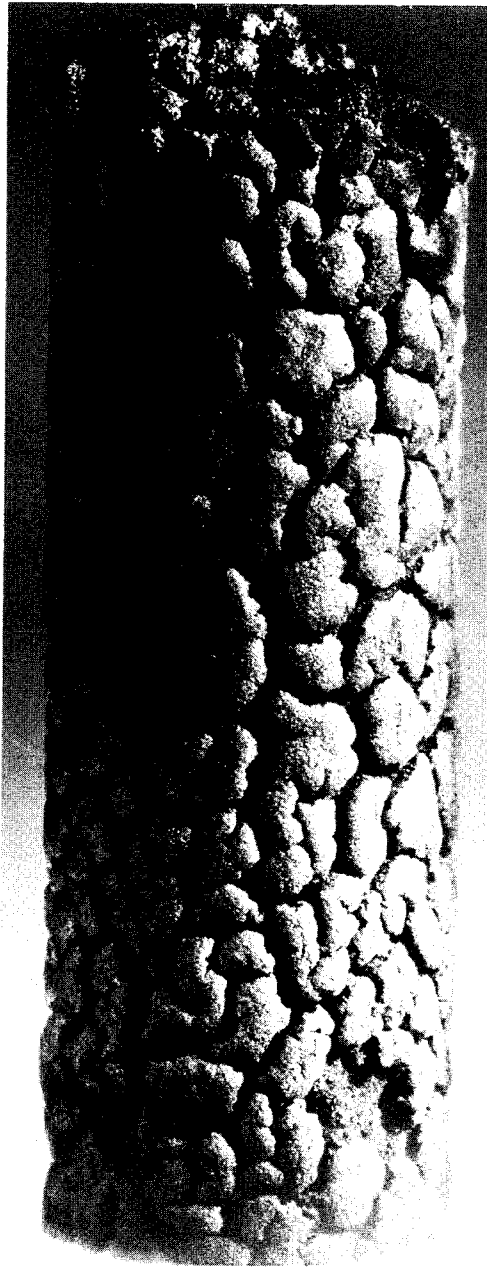
L-66-1119



(f) Test 7; large-grain model tested in air; $T_t = 36000$ R (20000 K); $t = 5.98$ sec.

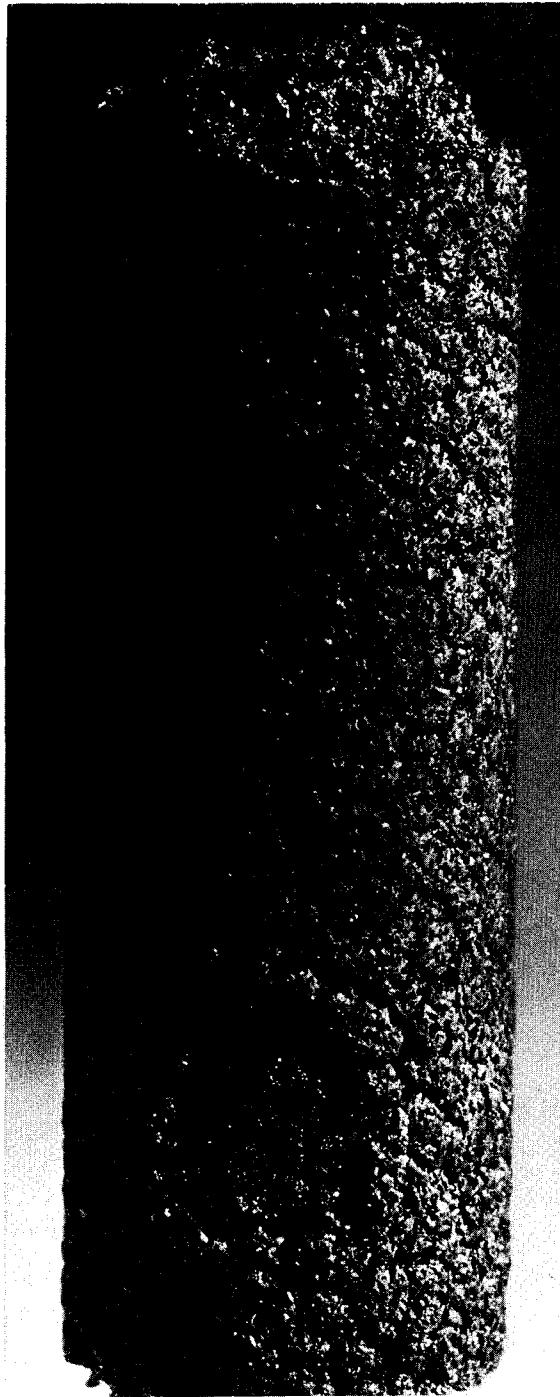
L-66-1120

Figure 6.- Continued.



(g) Test 9; small-grain model tested in N₂; $T_t = 35750^\circ \text{R}$ (19860° K); $t = 6.17$ sec. ^{L-66-1121}

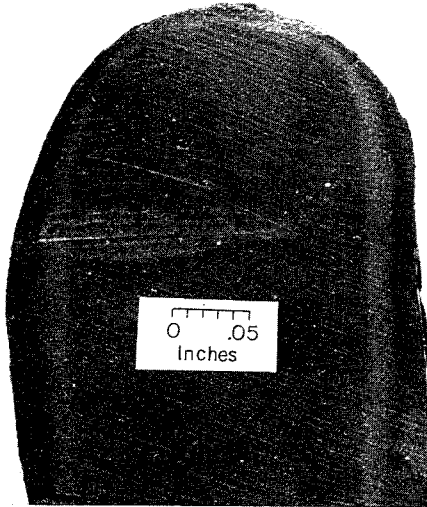
Figure 6.- Continued.



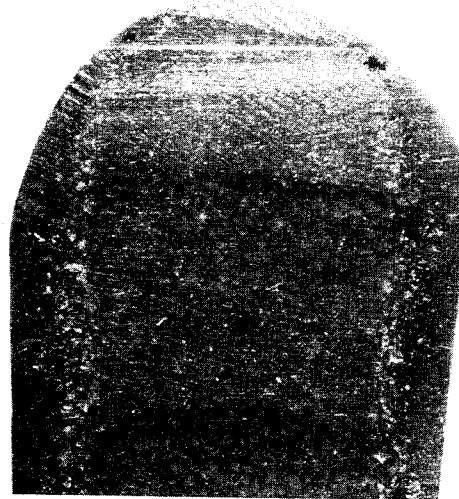
(h) Test 13; large-grain model tested in N_2 ; $T_t = 3575^\circ R$ ($1986^\circ K$); $t = 5.74$ sec. L-66-1122

Figure 6.- Concluded.

Tests in air



(a) Small-grain model;
test 3.

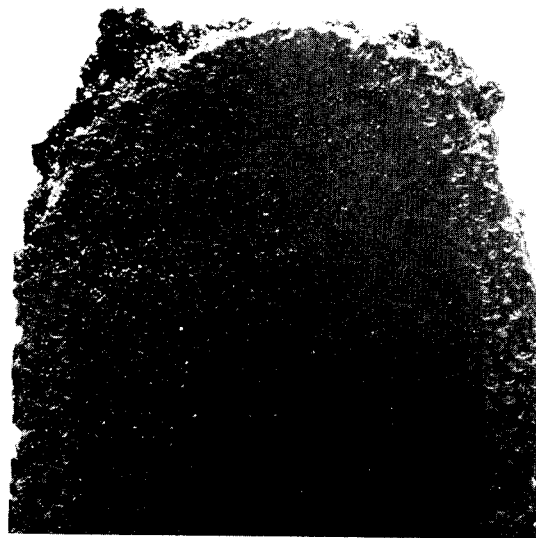


(b) Large-grain model;
test 7.

Tests in nitrogen



(c) Small-grain model;
test 11.



(d) Large-grain model;
test 13.

Figure 7.- Photographs of typical sectioned models. 3575°R (1986°K) $\leq T_f \leq 3600^{\circ}\text{R}$ (2000°K).

L-66-1123

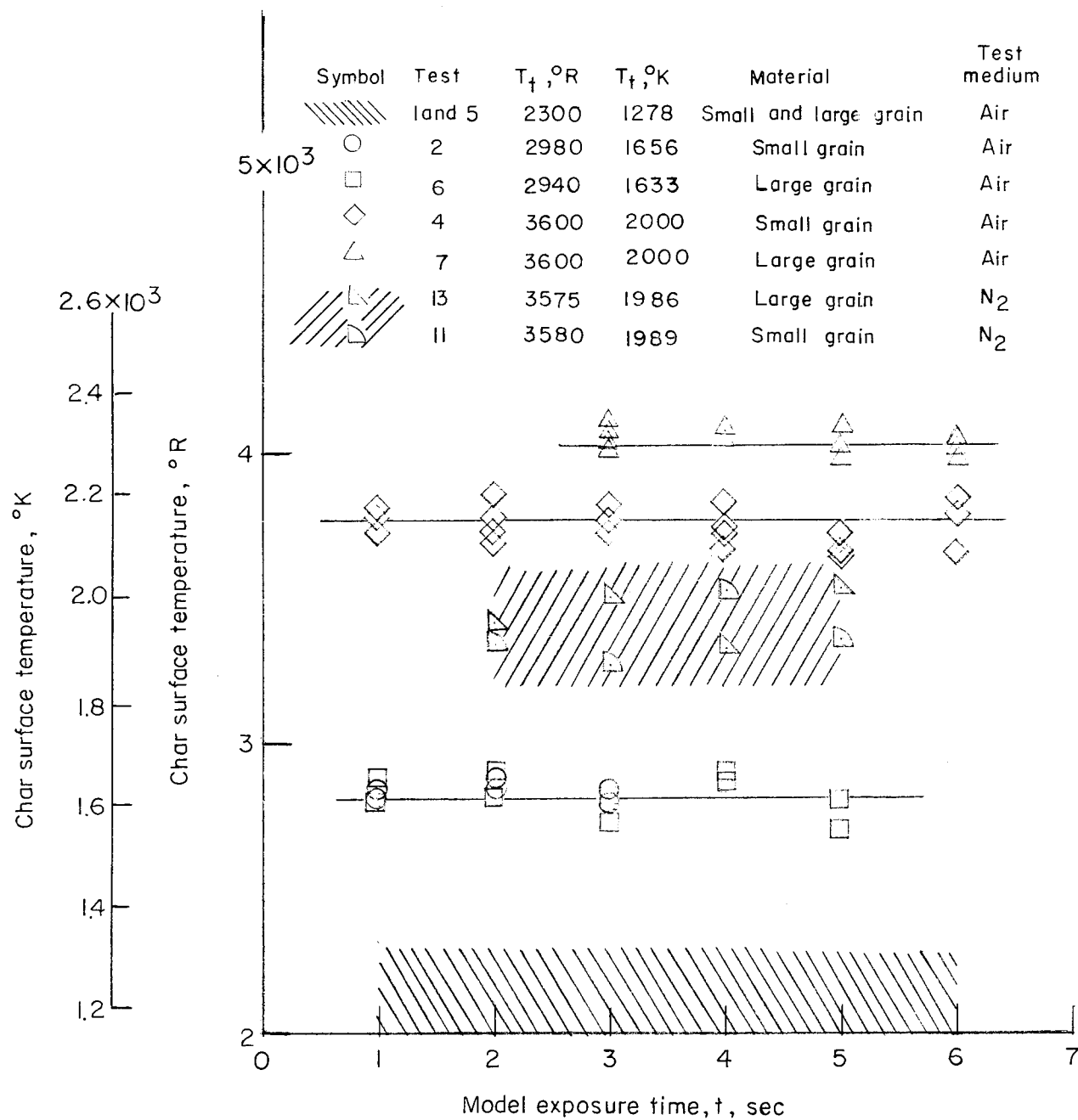
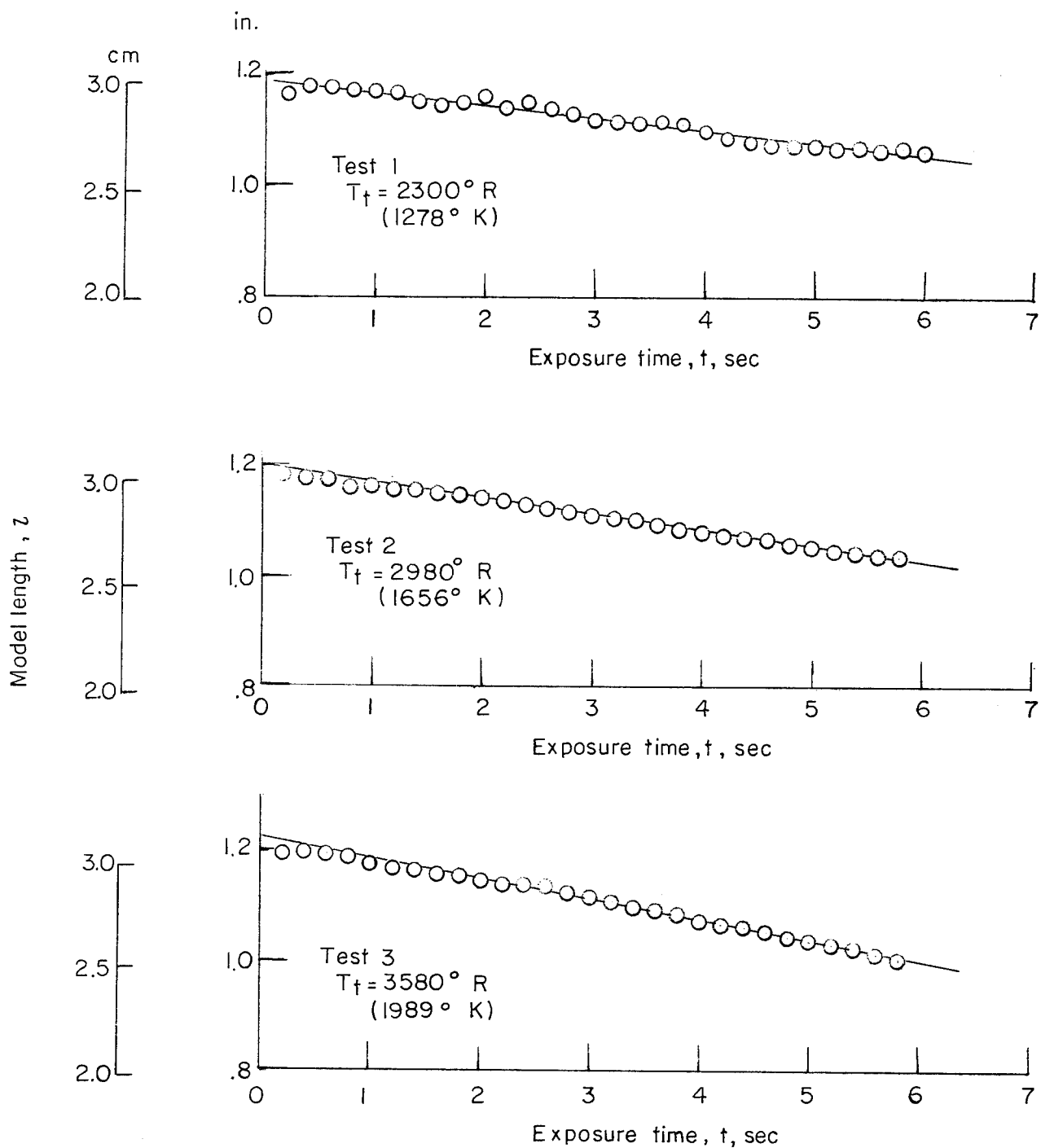
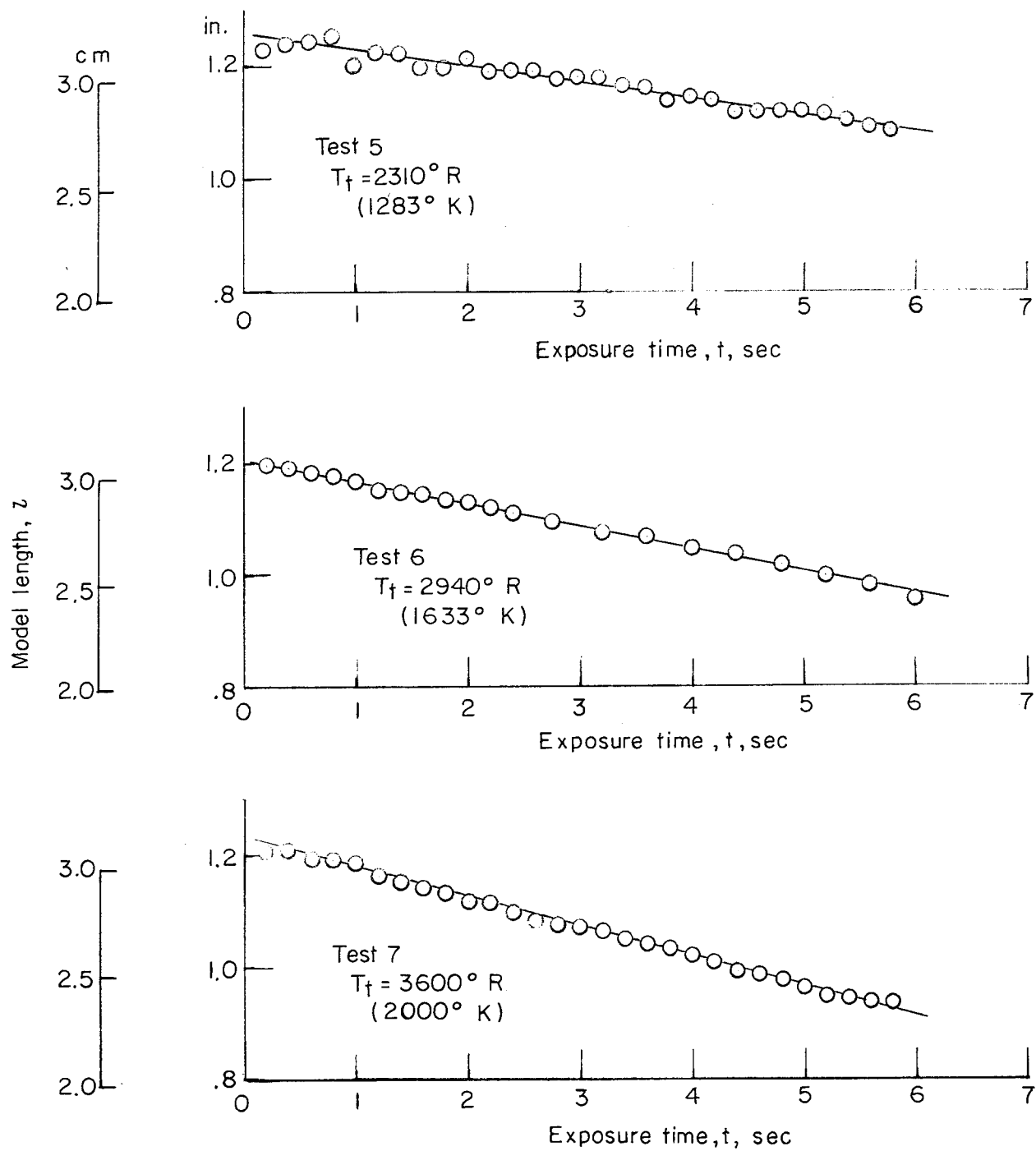


Figure 8.- Variation of char surface temperature with model exposure time. (Repeated symbols at a given t indicate measurements at different points on specimen nose.)



(a) Small-grain material tested in air.

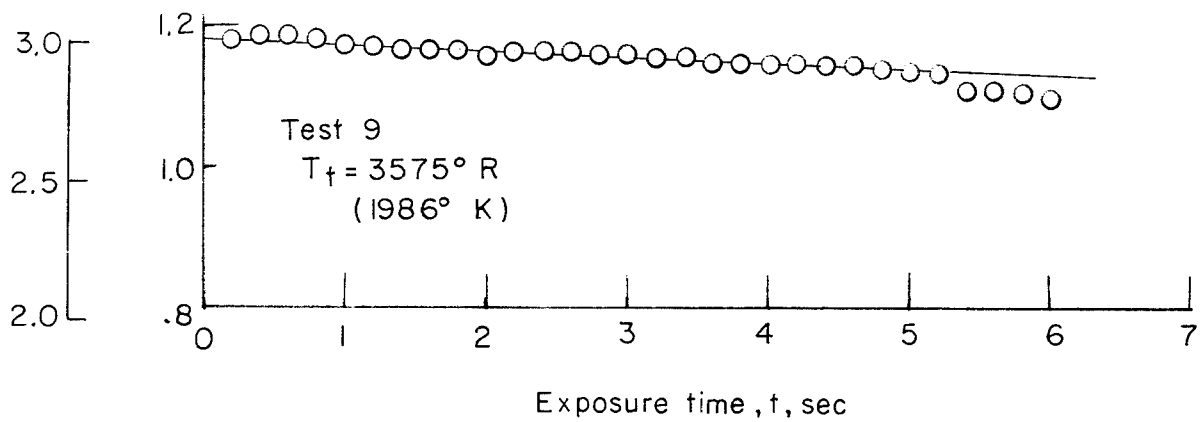
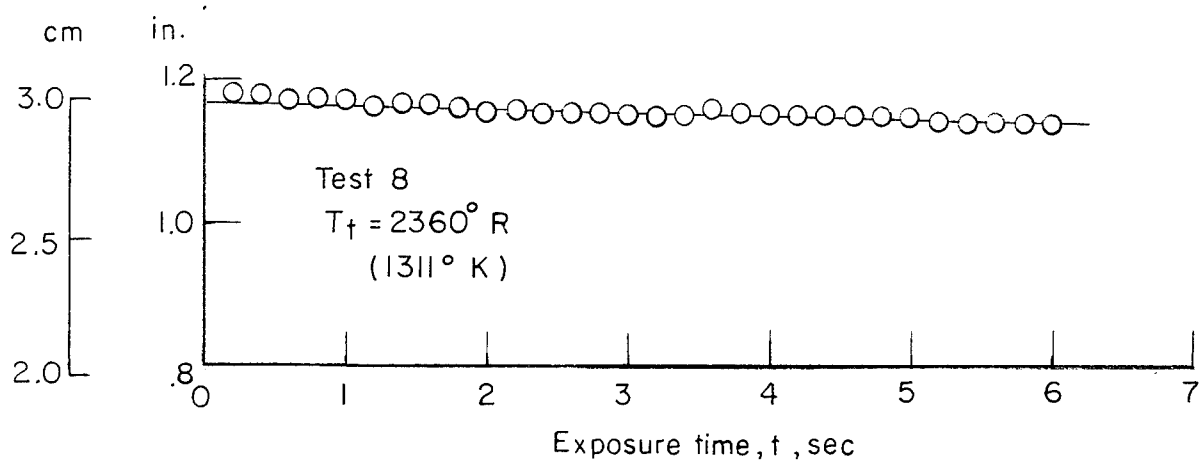
Figure 9.- Variation of model length with exposure time.



(b) Large-grain material tested in air.

Figure 9.- Continued.

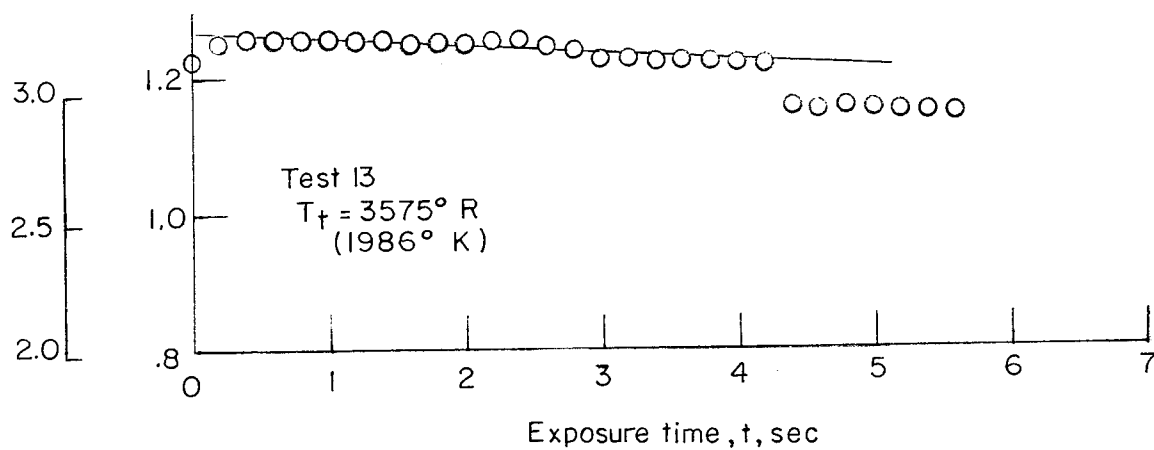
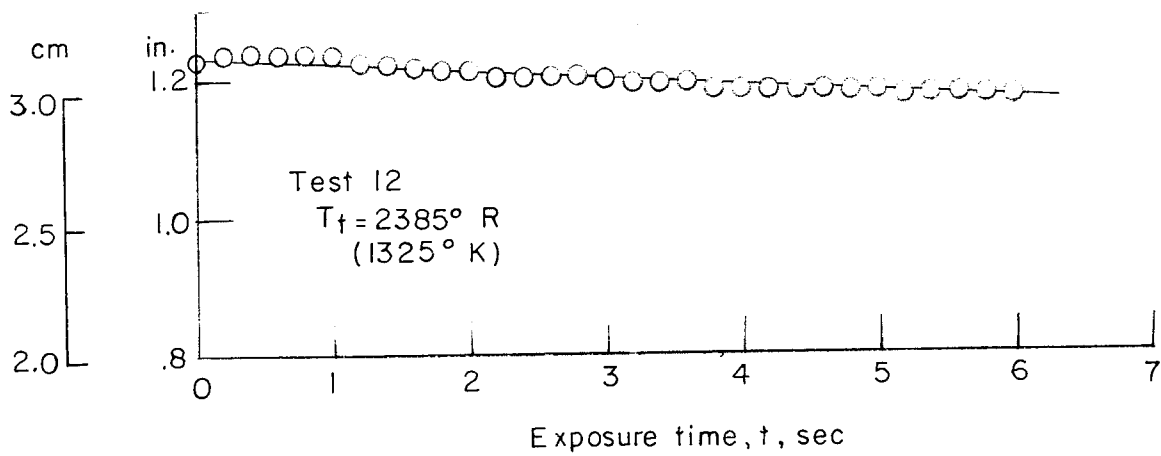
Model length, z



(c) Small-grain material tested in nitrogen.

Figure 9.- Continued.

Model length, z



(d) Large-grain material tested in nitrogen.

Figure 9.- Concluded.

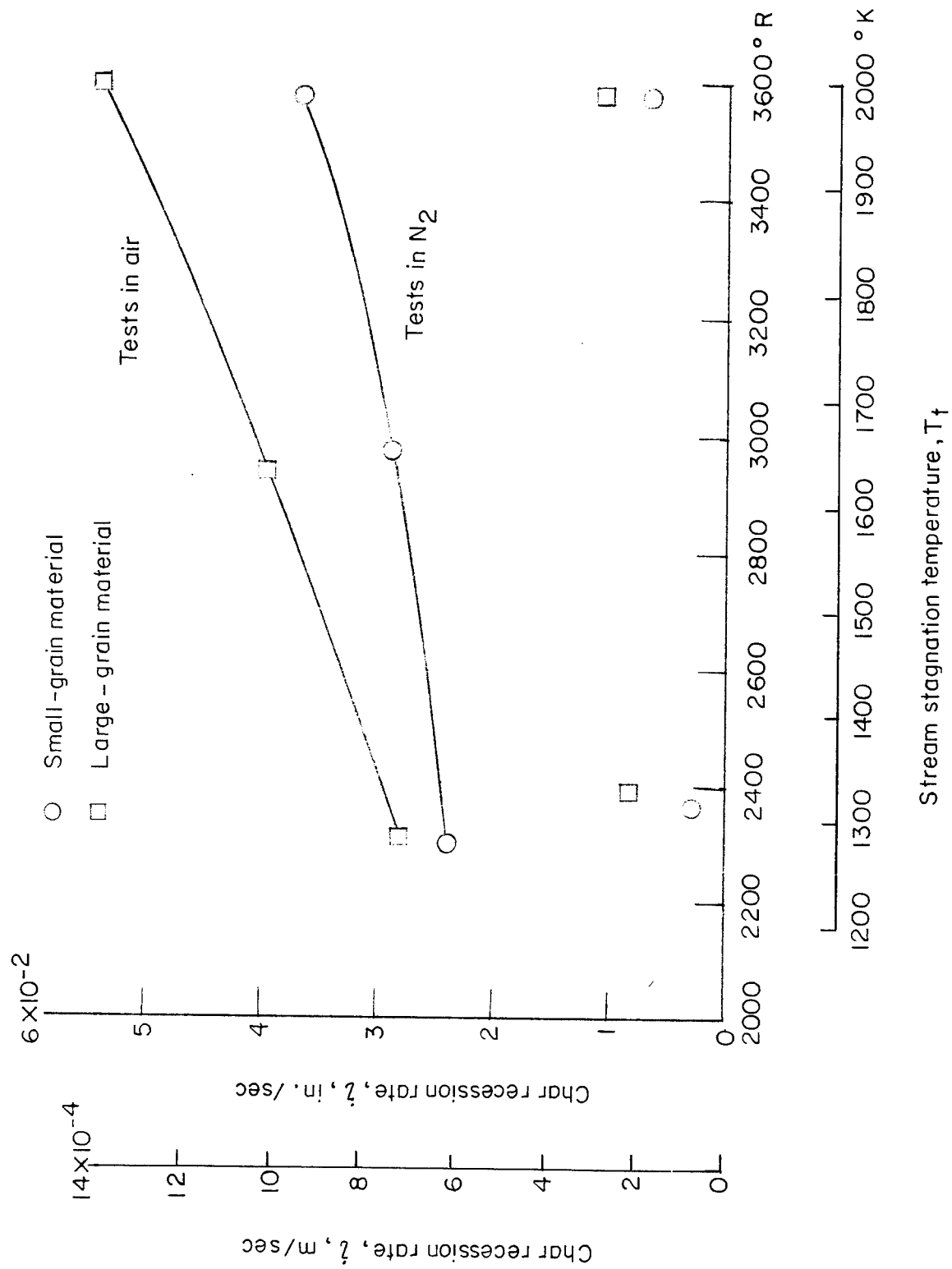


Figure 10.- Variation of char-layer recession rate with stream stagnation temperature.

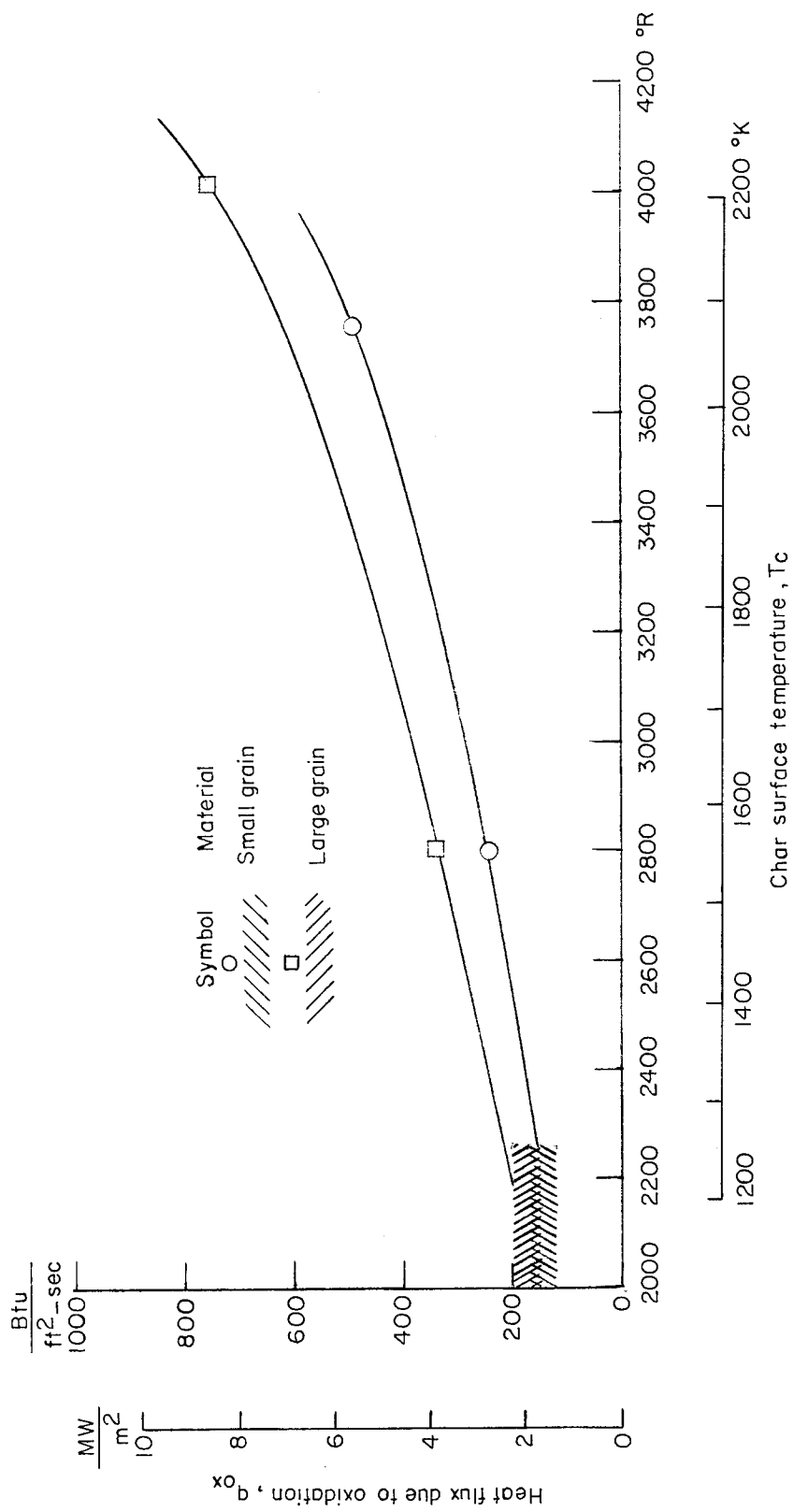


Figure 11.- Heat flux due to oxidation required to satisfy steady-state heat balance for tests in air.

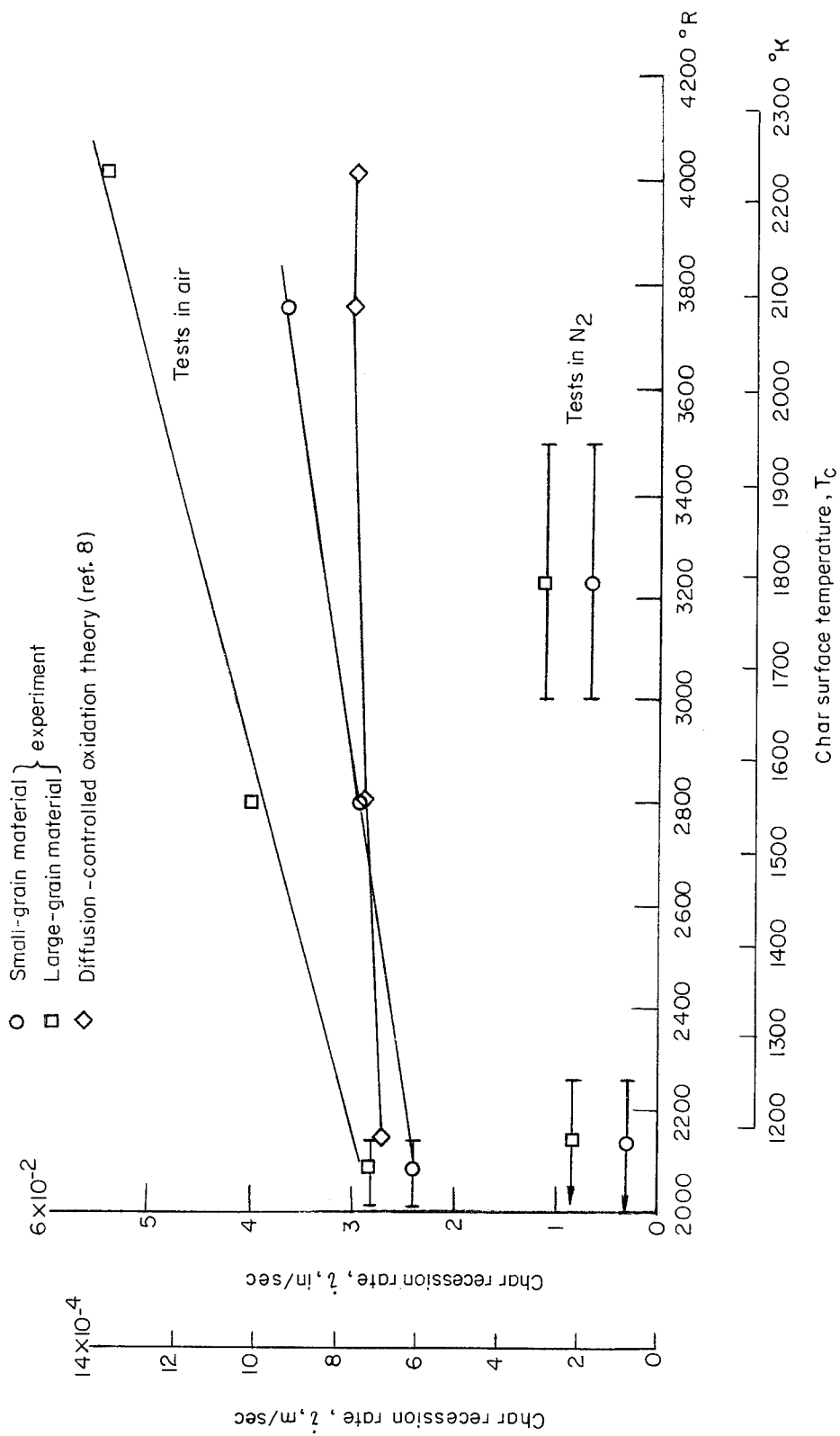


Figure 12.- Variation with char surface temperature of char-layer recession rate.